Inverse-mapped density-dependent relativistic mean-field inference of the neutron-star equation of state with terrestrial nuclear, NICER, and gravitational-wave constraints*

Jun-Hua Guo (郭俊华)[1,2†] Wen-Jie Xie (谢文杰)[3,4‡] Cheng-Jun Xia (夏铖君)[5§] Hai-Feng Liang (梁海锋)[1¶]

[1]Key laboratory for optical measurement and thin films of Shaanxi Province, Xi'an Technological University, Xi'an, Shaanxi 710021, China
[2]Department of Physics, Yuncheng University, Yuncheng 044000, China
[3]Shanxi Province Intelligent Optoelectronic Sensing Application Technology Innovation Center, Yuncheng University, Yuncheng 044000, China
[4]Department of Energy Engineering, Yuncheng University, Yuncheng 044000, China
[5]Center for Gravitation and Cosmology, College of Physical Science and Technology, Yangzhou University, Yangzhou 225009, China

Abstract: We perform a Bayesian inference of the cold dense-matter equation of state within a density-dependent relativistic mean-field (DD-RMF) model. The density-dependent couplings are reconstructed through an inverse mapping from a 12-dimensional set of nuclear-matter and high-density shape parameters. Two independent offsets, Δd_σ and Δd_ω, decouple the scalar and vector Typel–Wolter shift parameters from the isovector channel and provide a flexible isoscalar evolution at suprasaturation density. Thermodynamic consistency, beta stability, nonnegative core pressure, and the causal sound-speed condition are imposed on every accepted EOS. We analyze four likelihood combinations built from NICER mass–radius data, GW170817 tidal information, and heavy-ion collision flow constraints on the pressure of symmetric nuclear matter: NS-only, NS+HIC, NS+GW170817, and NS+HIC+GW170817. In the GW-conditioned comparison, the NS+HIC+GW170817 posterior gives $R_{1.4} = 11.91^{+0.37}_{-0.37}$ km, $R_{2.0} = 11.39^{+0.45}_{-0.51}$ km, and $M_{\max} = 2.123^{+0.084}_{-0.074}\,M_\odot$ at 68% credibility. HIC information narrows the high-density isoscalar sector and favors correlated scalar and vector density dependences. The posterior sensitivity tests identify the conversion of the reduced HIC density to physical density as an important systematic for the quantitative radius constraints.

Keywords: Inverse mapping, Density-dependent relativistic mean-field model, Dense-matter equation of state, Bayesian inference, Neutron stars

DOI: **CSTR:**

CPC Accepted

I. INTRODUCTION

Determining the equation of state (EOS) of cold, neutron-rich matter is a central problem connecting nuclear theory, laboratory experiments, and neutron-star (NS) astrophysics. The EOS enters the Tolman–Oppenheimer–Volkoff (TOV) equations and controls neutron-star masses and radii, while also affecting tidal responses in compact-binary inspirals [1−3]. Recent electromagnetic and multimessenger observations have made EOS inference increasingly quantitative, but they have also sharpened a basic modeling requirement: the high-density behavior inferred from neutron stars should remain connected to microphysical nuclear dynamics at and below saturation density [4−6]. Here this connection means that the core EOS is not fitted as a completely free pressure curve: its couplings are reconstructed from nuclear-matter properties at saturation and from controlled density-dependent coupling functions. It does not imply that the same core functional is used as a unified description of the outer crust.

Astrophysical observations provide the most direct constraints on the bulk pressure of cold beta-equilibrated matter. The existence of $\sim 2\,M_\odot$ neutron stars, first established for PSR J1614−2230 and later reinforced by measurements including PSR J0740+6620, requires sufficient high-density stiffness [7−9]. NICER pulse-profile modeling has added source-specific mass–radius information,

Received 28 August 2026; Accepted 26 October 2026

* This work is supported by the National Natural Science Foundation of China (Grant No. 12275234), the National SKA Program of China (Grant No. 2020SKA0120300), the Natural Science Basic Research Program of Shaanxi Provincial (Grant No. 2025JC-JCQN-093), the Innovation Capability Support Plan Program of Shaanxi Province (Grant No. 2025ZY1-GNYZ-05), and the Xi'an Science and Technology Program (Grant No. 24ZDCYJSGG0009).

† E-mail: junhuaguo@126.com
‡ E-mail: xiewenjie@ycu.edu.cn
§ E-mail: cjxia@yzu.edu.cn
¶ E-mail: lianghaifeng@xatu.edu.cn

©2027 Chinese Physical Society and the Institute of High Energy Physics of the Chinese Academy of Sciences and the Institute of Modern Physics of the Chinese Academy of Sciences and IOP Publishing Ltd. All rights, including for text and data mining, AI training, and similar technologies, are reserved.

beginning with PSR J0030+0451 and extending to the high-mass pulsar PSR J0740+6620 with improved background modeling and exposure [10−16]. A radius measurement for PSR J0437−4715 has further expanded the NICER dataset used in modern EOS analyses [17−19]. Gravitational-wave observations, especially GW170817, provide complementary information through tidal deformabilities and radii [20−23]. Together, these constraints have intensified the debate over how rapidly dense matter stiffens and whether the sound speed exceeds the conformal value $c_s^2 = 1/3$ inside massive neutron stars [24−26]. Bayesian EOS inference has therefore become a standard tool for propagating NICER, gravitational-wave, and massive-pulsar information into pressure, radius, and tidal-deformability constraints, using both parametric and nonparametric EOS representations [14, 27−30]. Machine-learning and emulator-based strategies have also been explored as fast inverse maps between observational data, microscopic EOS inputs, and neutron-star observables [31, 32].

Terrestrial nuclear information probes different density and isospin regimes and is therefore essential for breaking degeneracies left by neutron-star data alone. At sub- and near-saturation densities, chiral effective field theory (χEFT) provides a systematically improvable description of nuclear interactions and has become a standard low-density anchor for neutron-star matter [33−35]. Recent χEFT-based EOS constructions include quantified correlations across density, proton fraction, and temperature, enabling more controlled pressure bands for Bayesian inference [30, 36−38]. Because χEFT is a theory calculation rather than a laboratory measurement, its use in Bayesian analyses can range from a hard low-density prior to a reference band for assessing consistency. In the present work we adopt the latter choice, so that the impact of HIC information can be isolated from an additional low-density theory likelihood. Bayesian analyses of nuclear observables have also explored how symmetry-energy information can be propagated into neutron-rich matter constraints [39−43]. At intermediate and suprasaturation densities, heavy-ion collision (HIC) flow data constrain the pressure of nuclear matter under conditions inaccessible to static nuclei [44−47]. Recent work and Bayesian joint analyses have emphasized the complementarity between HIC information and neutron-star constraints [48−51]. Such joint analyses are particularly useful because HIC flow probes the isoscalar pressure of nearly symmetric matter, whereas neutron-star observables constrain beta-equilibrated matter through a combination of isoscalar and isovector physics. Studies of the basic properties of isospin-asymmetric matter provide an additional link between empirical nuclear parameters and neutron-star EOS predictions [52]. Nuclear structure observables, including PREX-2 and CREX neutron-skin measurements, provide additional information on isovector physics near saturation [53, 54], and have also been combined with neutron-star data in studies of the crust-core transition [55].

The challenge is to combine these heterogeneous constraints in a framework that is causal, thermodynamically consistent, and still interpretable at the level of microscopic interaction channels. Covariant density functional theory in the relativistic mean-field (RMF) approximation is well suited to this task because it describes nuclear saturation through the balance of large scalar attraction and vector repulsion [56−59]. Calibrated RMF interactions such as NL3 and FSUGold have demonstrated the phenomenological power of this approach in finite nuclei and nuclear matter [60, 61]. In density-dependent RMF (DD-RMF) models, medium effects are encoded through density-dependent couplings, while the rearrangement term preserves thermodynamic consistency [62−64]. For neutron-star applications, however, the extrapolation of the isovector sector and the suprasaturation evolution of the scalar and vector couplings remain major sources of uncertainty.

In this work we develop a Bayesian DD-RMF inference framework designed to expose how neutron-star and terrestrial nuclear data constrain different parts of the interaction. Rather than sampling the density dependence of the couplings as unconstrained functions, we use an inverse-mapping construction in which saturation-scale nuclear-matter properties, isovector parameters, high-density asymptotic coupling limits, and two independent isoscalar shift offsets uniquely determine the scalar, vector, and isovector Typel–Wolter–type coupling functions [62, 63]. The offsets Δd_σ and Δd_ω allow the scalar and vector density dependences to vary independently of the isovector shift, reducing artificial locking between interaction channels. This extends the common-shift construction used in our previous inverse-mapping study [65, 66] by allowing the high-density scalar attraction and vector repulsion to respond separately to the data. This channel-resolved construction is useful because an RMF EOS is not determined by a pressure curve alone. The same beta-equilibrated pressure can arise from different cancellations between the large scalar attraction and vector repulsion, whereas HIC flow information acts directly on the isoscalar pressure of symmetric matter. The inverse mapping therefore lets us ask a more microscopic question: whether adding HIC information selects a particular density evolution of the scalar and vector mean fields, and how that selection propagates to neutron-star radii and tidal responses.

We confront the resulting EOS ensemble with four data selections. The NS-only run uses source-specific, mass-marginalized kernel-density estimates of the NICER mass–radius posteriors for PSR J0030+0451, PSR J0740+6620, and PSR J0437−4715. The HIC+NS run adds the heavy-ion flow constraint on the pressure of

CPC Accepted

symmetric nuclear matter at intermediate density. Two parallel runs, NS+GW170817 and HIC+NS+GW170817, additionally include the GW170817 tidal-deformability likelihood. In all selections we do not add a separate maximum-mass likelihood, avoiding double use of the Shapiro-delay mass information already included in the PSR J0740+6620 NICER posterior. Low-density χEFT pressure bands are shown only as external references and do not enter the likelihood. Posterior sampling is performed with MultiNest nested sampling [67, 68].

The remainder of this paper is organized as follows. In Sec. II we present the DD-RMF model, the inverse mapping, the beta-equilibrated EOS construction, and the likelihood. Section III discusses the inferred nuclear parameters, reconstructed coupling functions, EOS bands, and neutron-star observables. We conclude in Sec. IV with a summary and outlook.

II. THEORETICAL FRAMEWORK

A. Density-dependent relativistic mean-field model and inverse mapping

We adopt a density-dependent relativistic mean-field (DD-RMF) energy-density functional for cold, uniform matter. Relativistic mean-field models provide a compact and microphysically interpretable description of nuclear saturation in terms of large scalar and vector self-energies [56−59]. In DD-RMF, medium effects are encoded through explicit density dependence of the effective couplings while preserving thermodynamic consistency via the rearrangement contribution [62, 69, 70]. For broad context on covariant parameterizations under empirical nuclear-matter constraints, see Ref. [71]; throughout this work, we use natural units $\hbar = c = 1$.

For uniform matter composed of neutrons (n) and protons (p) with number densities n_n and n_p, we define the total baryon density $n \equiv n_n + n_p$, the isovector density $n_3 \equiv n_p - n_n$, and the proton fraction $x_p \equiv n_p/n$. With this sign convention, neutron-rich matter has $n_3 < 0$, and only n_3^2 enters the static isovector energy density, whereas the sign is relevant in the proton and neutron chemical potentials. The Dirac effective mass is expressed as $M^*(n_n, n_p) = m_N - \Sigma_S$, where $\Sigma_S = G_\sigma(n) n_s$ is the scalar self-energy. The total scalar density is given by $n_s = \sum_{i=n,p} n_{s,i}$, with

$$n_{s,i} = \frac{2}{(2\pi)^3} \int_0^{k_{F,i}} d^3k \, \frac{M^*}{\sqrt{k^2 + M^{*2}}}. \tag{1}$$

The kinetic (nucleonic) energy density ε_N and pressure P_N are evaluated via the standard integrals over the Fermi sea:

$$\varepsilon_N = \sum_{i=n,p} \frac{2}{(2\pi)^3} \int_0^{k_{F,i}} d^3k \, \sqrt{k^2 + M^{*2}}, \tag{2}$$

$$P_N = \sum_{i=n,p} \frac{2}{3(2\pi)^3} \int_0^{k_{F,i}} d^3k \, \frac{k^2}{\sqrt{k^2 + M^{*2}}}. \tag{3}$$

The interaction (mean-field) contribution is written in a compact point-coupling form,

$$\varepsilon_{\rm int} = \frac{1}{2} G_\sigma(n) n_s^2 + \frac{1}{2} G_\omega(n) n^2 + \frac{1}{2} G_\rho(n) n_3^2, \tag{4}$$

which is equivalent to the usual meson-exchange formulation at the mean-field level after identifying the effective couplings $G_i(n) \equiv g_i^2(n)/m_i^2$ for the σ, ω, and ρ mesons [62−64]. Crucially, the density-dependent couplings introduce a rearrangement self-energy [62, 69],

$$\Sigma_R(n) = \frac{1}{2} n^2 \frac{dG_\omega}{dn} - \frac{1}{2} n_s^2 \frac{dG_\sigma}{dn} + \frac{1}{2} n_3^2 \frac{dG_\rho}{dn}, \tag{5}$$

which must be included in both the pressure and the chemical potentials to maintain thermodynamic consistency.

To describe the density dependence of the couplings, we write $G_i(n) = G_{i0} f_i^2(n)$ for $i \in \{\sigma, \omega, \rho\}$, where $G_{i0} \equiv G_i(n_0)$ is the coupling strength at saturation density, and the shape functions $f_i(n)$ satisfy $f_i(n_0) = 1$. Following the Typel–Wolter ansatz [62], we adopt a rational form:

$$f_i(n) = a_i \frac{1 + b_i (x + d_i)^2}{1 + c_i (x + d_i)^2}, \qquad x \equiv n/n_0, \tag{6}$$

which naturally approaches an asymptotic limit $f_{i,\infty} \equiv \lim_{x\to\infty} f_i(x) = a_i(b_i/c_i)$ at high densities.

Instead of freely varying the microscopic coefficients a_i, b_i, c_i, and d_i, our inference is performed in a physically intuitive 12-dimensional parameter space:

$$\boldsymbol{\theta} = \big(K_0,\, (M^*/m_N)_0,\, n_0,\, E_0,\, E_{\rm sym,0},\, L,\, K_{\rm sym},\, f_{\sigma,\infty},\, f_{\omega,\infty},\, f_{\rho,\infty},\, \Delta d_\sigma,\, \Delta d_\omega\big). \tag{7}$$

Here, $E_0 \equiv (E/A)(n_0) - m_N$ is the binding energy per nucleon at n_0, where m_N denotes the free nucleon mass and is distinct from the neutron-star gravitational mass M. These empirical parameters are defined in the standard way by expanding the energy per baryon $E(n, \delta)$ around saturation with respect to density and the isospin asymmetry parameter $\delta \equiv (n_n - n_p)/n$ [43, 52, 72]. Specifically, K_0 is the incompressibility of symmetric nuclear matter at n_0, $(M^*/m_N)_0$ is the Dirac effective-mass ratio at saturation, $E_{\rm sym,0}$ is the symmetry energy at n_0, $L = 3n_0(dE_{\rm sym}/dn)_{n_0}$ is its slope, and $K_{\rm sym} = 9n_0^2(d^2E_{\rm sym}/dn^2)_{n_0}$ is its curvature. The quantities $f_{\sigma,\infty}$, $f_{\omega,\infty}$, and $f_{\rho,\infty}$ are the high-density limits of the normalized scalar, vector, and isovector coupling functions, respectively. The parameters Δd_σ and

CPC Accepted

Δd_ω are offsets of the scalar and vector Typel–Wolter shift parameters relative to the isovector shift. The first ten entries describe the saturation-scale and asymptotic properties of the interaction, while the last two parameters allow the scalar and vector shift parameters to differ from the isovector one. This construction increases the flexibility of the high-density isoscalar sector without abandoning the deterministic connection between empirical nuclear-matter inputs and microscopic coupling functions.

To connect this macroscopic parameter space to the microscopic effective couplings, we employ a numerical inverse mapping procedure. The coupling strengths at saturation ($G_{\sigma0}, G_{\omega0}, G_{\rho0}$) are analytically fixed by the effective mass, binding energy, and symmetry energy, respectively. The density-dependence shape parameters are subsequently determined by matching the specified isovector properties ($L, K_{\rm sym}$), the isoscalar properties (K_0 and the zero-pressure condition at saturation), the three asymptotic coupling limits, and the two independent isoscalar shift offsets. After fixing the coupling strengths at saturation, the isoscalar and isovector density-shape parameters are solved jointly. At each trial of these parameters, the scalar field equation is solved anew at every density used to evaluate the symmetry-energy derivatives. Thus the density dependence of the effective mass, including its contribution to the kinetic symmetry energy, follows from the current scalar coupling function. It is not inferred from the effective mass at saturation alone. The detailed step-by-step mathematical derivation of this inverse mapping is provided in Appendix A. The construction uses finite acceptance thresholds for the matching residuals, rather than imposing exact algebraic equality. The internal residual audit and the distinction between acceptance thresholds and derivative accuracy are described in Appendix A.

B. Equation of state and neutron-star structure

With the model parameters determined, we compute the core EOS by imposing cold β equilibrium and charge neutrality at each baryon density n: $\mu_n = \mu_p + \mu_e$, $\mu_e = \mu_\mu$, and $n_p = n_e + n_\mu$. The nucleon chemical potentials explicitly include the rearrangement term:

$$\boldsymbol{\mu}_{n,p} = E^*_{F,n,p} + G_\omega(n)\,n \mp G_\rho(n)\,n_3 + \Sigma_R(n), \tag{8}$$

where $E^*_{F,i} = \sqrt{k^2_{F,i} + M^{*2}}$, and the leptons (e,μ) are treated as free Fermi gases. For a given density n, we solve for the proton fraction $x_p(n)$ and subsequently evaluate the total energy density $\varepsilon(n) = \varepsilon_N + \varepsilon_{\rm int} + \varepsilon_\ell$ and the total pressure $P(n)$. Numerically, we obtain the pressure directly from the thermodynamic relation $P(n) = n(d\varepsilon/dn) - \varepsilon(n)$ using finite-difference derivatives on the computed $\varepsilon(n)$ to guarantee exact thermodynamic consistency.

To describe the outer layers of the neutron star, we attach a tabulated crust EOS based on the SLy4 functional [73]. The transition point between the crust and the core is identified by enforcing continuity and monotonicity of $P(\varepsilon)$ across the interface [5, 6, 55]. This crust prescription provides a standard low-density completion of the stellar EOS and is not an additional constraint on the inverse mapping of the uniform core functional. The core EOS remains connected to nuclear microphysics through the saturation properties in Eq. (7), the density-dependent RMF structure, and the external comparison with low-density χEFT bands. The attached crust mainly affects the outer stellar layers and does not determine the high-density isoscalar response discussed below. Furthermore, we filter unphysical EOS models by enforcing causality, requiring that the squared speed of sound $c_s^2 = dP/d\varepsilon \le 1$ throughout the entire density range.

The macroscopic structure of a non-rotating neutron star is obtained by integrating the TOV equations [1, 74]:

$$\frac{dP}{dr} = -\frac{(\varepsilon + P)\left[m(r) + 4\pi r^3 P\right]}{r\left[r - 2m(r)\right]}, \tag{9}$$

$$\frac{dm}{dr} = 4\pi r^2 \varepsilon(r), \tag{10}$$

subject to the central boundary conditions $m(0) = 0$ and $P(0) = P_c$. The stellar radius R is defined at the surface where $P(R) = 0$, yielding the gravitational mass $M = m(R)$. Scanning over a grid of central pressures produces the stable M–R sequence and identifies the maximum mass $M_{\rm max}$ [4, 5]. For comparisons with gravitational-wave data, the tidal deformability is computed alongside the structure equations following standard methods [2, 3].

C. Bayesian inference and observational constraints

We employ Bayesian inference to confront the generated EOS models with NICER mass–radius data, GW170817 tidal information, and terrestrial HIC pressure information [41, 65, 66, 70, 75]. The posterior distribution $p(\boldsymbol{\theta}|\mathcal{D})$ is proportional to the product of the prior $\pi(\boldsymbol{\theta})$ and the combined likelihood $\mathcal{L}(\boldsymbol{\theta})$. We sample the posterior using the nested sampling algorithm [67, 76] implemented via `MultiNest` [68]. The total log-likelihood is constructed as a modular sum of contributions from distinct data sectors. For the present analysis we use four NS-containing combinations: NS-only, HIC+NS, NS+GW170817, and HIC+NS+GW170817. NS-only defines the NICER baseline, HIC+NS tests the response to an intermediate-density symmetric-matter pressure constraint, and the two GW170817 runs test how the same EOS family responds when tidal-deformability information is added. To avoid reusing the PSR J0740+6620 Shapiro-delay mass information both

CPC Accepted

through the NICER mass–radius posterior and through a separate massive-pulsar existence term, the fiducial runs use

$$\ln\mathcal{L}_{\rm NS-only} = \ln\mathcal{L}_{\rm NS}, \qquad \ln\mathcal{L}_{\rm HIC+NS} = \ln\mathcal{L}_{\rm NS} + \ln\mathcal{L}_{\rm HIC}, \tag{11}$$

$$\ln\mathcal{L}_{\rm NS+GW170817} = \ln\mathcal{L}_{\rm NS} + \ln\mathcal{L}_{\rm GW170817},$$
$$\ln\mathcal{L}_{\rm HIC+NS+GW170817} = \ln\mathcal{L}_{\rm NS} + \ln\mathcal{L}_{\rm HIC} + \ln\mathcal{L}_{\rm GW170817}. \tag{12}$$

For the astrophysical observations ($\ln\mathcal{L}_{\rm NS}$), we incorporate NICER pulse-profile constraints for PSR J0030+0451 [10, 11], PSR J0740+6620 [12, 13, 16], and PSR J0437−4715 [17]. For each source, the observational posterior in the (R, M) plane is represented using a two-dimensional kernel density estimate (KDE), $\hat{p}_s(R, M)$. In the present analysis, the EOS is compared with each individual source through a source-specific mass-marginalized likelihood, rather than by averaging the KDE over the entire stable M–R branch. The NS contribution is

$$\ln\mathcal{L}_{\rm NS} = \sum_s \ln\mathcal{L}_{\rm NS}^{(s)}, \qquad \mathcal{L}_{\rm NS}^{(s)} = \frac{\int_{M_{\rm lo}^{(s)}}^{M_{\rm hi}^{(s)}} \tilde{p}_s(M)\,dM}{M_{\rm hi}^{(s)} - M_{\rm lo}^{(s)}}, \tag{13}$$

with the EOS-dependent support function

$$\tilde{p}_s(M) = \begin{cases} \hat{p}_s[R_{\rm EOS}(M), M], & M \le M_{\rm max} \text{ on the stable branch} \\ 0, & M > M_{\rm max}. \end{cases} \tag{14}$$

Here $M_{\rm lo}^{(s)}$ and $M_{\rm hi}^{(s)}$ are taken from the central mass range of the corresponding NICER posterior samples. In the numerical implementation we use the 0.5 and 99.5 percentiles of the mass samples and perform the integral on a uniform mass grid. Equation (14) also specifies how the likelihood is evaluated if the observational mass window extends beyond the maximum stable mass supported by the EOS: the unsupported part of the fixed observational mass interval contributes zero KDE weight, while the normalization remains the full observational width $M_{\rm hi}^{(s)} - M_{\rm lo}^{(s)}$, not a truncated EOS-dependent width. The production likelihood uses fixed effective NICER KDE products in the $(R\,[\rm km], M\,[M_\odot])$ plane. Following the posterior-density treatment of Raaijmakers et al. [77], we use these posterior samples as effective observational likelihood densities and do not attempt to reconstruct or divide out the internal priors used by the original pulse-profile analyses. For GW170817, the TOV calculation is supplemented by the tidal Love-number equations and yields the dimensionless tidal deformability curve $\Lambda_{\rm EOS}(M)$. We use an event-level likelihood proxy in the space of mass ratio and component tidal deformabilities. For a fixed chirp mass $\mathcal{M} = 1.186\,M_\odot$, the component masses are written as

$$M_1(q) = \mathcal{M} q^{-3/5}(1+q)^{1/5}, \qquad M_2(q) = q\,M_1(q), \tag{15}$$

where $q = M_2/M_1 \le 1$. The GW170817 contribution is obtained by interpolating $\Lambda_{\rm EOS}(M_1)$ and $\Lambda_{\rm EOS}(M_2)$ on the stable branch and integrating the event likelihood over the allowed mass-ratio interval,

$$\ln\mathcal{L}_{\rm GW170817} = \ln\int dq\,\mathcal{L}_{\rm event}\left[q, \Lambda_{\rm EOS}(M_1(q)), \Lambda_{\rm EOS}(M_2(q))\right]. \tag{16}$$

EOS samples for which the required component masses or tidal deformabilities cannot be evaluated on the stable branch receive negligible likelihood. For the GW170817 likelihood, we use the event-level posterior-density proxy associated with the low-spin phenomenological-PNRT analysis. We fix the source-frame chirp mass to $\mathcal{M} = 1.186\,M_\odot$, integrate over the mass ratio on 200 equally spaced points, use the central 0.5–99.5 percentile range of the mass-ratio samples clipped to $0.60 \le q \le 0.995$, and retain the support $0 \le \Lambda_{1,2} \le 20000$. The original mass-ratio prior $p(q|\mathcal{M}) \propto (1+q)^{2/5} q^{-6/5}$ is divided out, while the stated tidal-deformability support is retained. No separate $M_{\rm max}$ term is included in the fiducial likelihood. An optional maximum-mass consistency term, $\ln\mathcal{L}_{M_{\rm max}}$ [7–9, 78], is implemented only as a lower-bound/existence constraint,

$$\ln\mathcal{L}_{M_{\rm max}} = \begin{cases} -\frac{1}{2}\left(\frac{2.08\,M_\odot - M_{\rm max}}{0.07\,M_\odot}\right)^2, & M_{\rm max} < 2.08\,M_\odot, \\ 0, & M_{\rm max} \ge 2.08\,M_\odot. \end{cases} \tag{17}$$

Thus EOSs above the reference mass receive no penalty from $\ln\mathcal{L}_{M_{\rm max}}$. This optional term is not included in the fiducial data selections, because the NICER J0740 posterior already incorporates the radio Shapiro-delay mass information. A full hierarchical treatment would model the observed neutron-star mass distribution jointly with the EOS, as in Ref. [79], and we leave such a population-level extension to future work. Unless explicitly stated otherwise, all data combinations reported in Sec. III set $\ln\mathcal{L}_{M_{\rm max}} = 0$.

For the HIC pressure-band constraint, we define the tabulated midpoint and width at the sampled reduced density point j as

CPC Accepted

$$\bar{P}_{\mathrm{HIC},j}=\frac{P^{\max}_{\mathrm{HIC},j}+P^{\min}_{\mathrm{HIC},j}}{2},\qquad \sigma_{\mathrm{HIC},j}=\frac{P^{\max}_{\mathrm{HIC},j}-P^{\min}_{\mathrm{HIC},j}}{2}, \quad (18)$$

and use a Gaussian pressure-band likelihood, up to additive constants independent of the EOS parameters,

$$\ln\mathcal{L}_{\mathrm{HIC}}=-\frac{1}{2}\sum_{j}\left[\frac{P_{\mathrm{SNM}}(u_j n_0)-\bar{P}_{\mathrm{HIC},j}}{\sigma_{\mathrm{HIC},j}}\right]^2. \quad (19)$$

Here P_{SNM} is the symmetric-matter pressure obtained from the same DD-RMF functional by setting $n_p=n_n=n/2$. The HIC density coordinate is $u_j=n/n_0$, so the model pressure is evaluated at $n=u_j n_0$ for each sampled EOS. In the production calculation, the fiducial HIC likelihood is evaluated only on the 15-point grid with $2.0\le u_j\le 4.5$. The lower and upper pressure boundaries are obtained by linear interpolation of the supplied pressure-band data. In the default likelihood, u is interpreted as density measured relative to the saturation point of the same sampled EOS. We use that sample's inferred n_0 in the conversion $n=un_0$. This convention keeps the reduced-density coordinate consistent with the density scale used to construct each inverse-mapped EOS and avoids imposing an additional external value of n_0 on a parameter that is sampled in the model. It is nevertheless a modeling choice rather than a unique conversion of the flow band. We define a fixed-n_0 test in which only the HIC coordinate conversion is changed to $n=un_0^{\mathrm{ref}}$ with $n_0^{\mathrm{ref}}=0.16\ \mathrm{fm}^{-3}$. The EOS saturation density n_0 and all other 11 EOS parameters remain sampled with the same priors, and the NS, HIC-pressure, and GW170817 likelihood prescriptions are otherwise unchanged.

In the production calculations, MultiNest is run in the 12-dimensional parameter space with 2000 live points. Samples that fail the inverse mapping, the fast pressure-stability filter, the TOV construction, or the causal sound-speed condition are assigned negligible likelihood and do not contribute to the posterior ensembles. To isolate the structural role of the two independent isoscalar offsets, we also compare with a matched 10-dimensional control in which $\Delta d_\sigma=\Delta d_\omega=0$. The resulting posterior comparison quantifies the effect of relaxing the common-shift assumption.

III. RESULTS AND DISCUSSIONS

A. Posterior constraints on nuclear parameters

We begin by examining the marginalized posterior distributions in the 12-dimensional parameter space. Table 1 summarizes the uniform prior ranges and the 68% and 90% credible intervals for the NS+GW170817 and NS+HIC+GW170817 analyses. Figure 1 shows the corresponding one-dimensional posterior distributions, while Figs. 2 and 3 display the two-dimensional correlations for the two GW-conditioned data selections.

The saturation-scale parameters K_0, E_0, $E_{\mathrm{sym},0}$, L, and K_{sym} remain comparatively broad. This behavior is expected because the NICER mass–radius and GW170817 tidal likelihoods constrain the bulk relation $P(\varepsilon)$ more directly than the decomposition of the EOS into individual nuclear-matter coefficients. The HIC pressure band acts mainly on the intermediate-density isoscalar pressure, and therefore does not by itself turn the near-saturation isovector parameters into sharply measured quantities. In particular, the NS+HIC+GW170817 posterior gives $L=44.6^{+24.2}_{-27.8}$ MeV and $K_{\mathrm{sym}}=-328.3^{+175.2}_{-169.4}$ MeV at 68% credibility, reflecting substantial remaining freedom in the symmetry energy.

Table 1. Prior ranges and marginalized credible intervals for the 12 parameters of the stable density-dependent RMF model.

Parameter	Prior	NS+GW 68% C.I.	NS+GW 90% C.I.	NS+HIC+GW 68% C.I.	NS+HIC+GW 90% C.I.
K_0(MeV)	$\mathcal{U}(200.0,280.0)$	$233.8^{+27.5}_{-22.0}$	$233.8^{+38.8}_{-29.7}$	$233.1^{+27.7}_{-22.4}$	$233.1^{+39.7}_{-29.8}$
$(M^*/m_N)_0$	$\mathcal{U}(0.400,0.700)$	$0.545^{+0.062}_{-0.059}$	$0.545^{+0.089}_{-0.082}$	$0.532^{+0.066}_{-0.055}$	$0.532^{+0.095}_{-0.073}$
$n_0\ (\mathrm{fm}^{-3})$	$\mathcal{U}(0.1350,0.1800)$	$0.1639^{+0.0118}_{-0.0180}$	$0.1639^{+0.0148}_{-0.0246}$	$0.1470^{+0.0080}_{-0.0069}$	$0.1470^{+0.0134}_{-0.0099}$
E_0(MeV)	$\mathcal{U}(-17.00,-15.50)$	$-16.25^{+0.46}_{-0.46}$	$-16.25^{+0.64}_{-0.64}$	$-16.23^{+0.49}_{-0.50}$	$-16.23^{+0.65}_{-0.68}$
$E_{\mathrm{sym},0}$(MeV)	$\mathcal{U}(26.00,38.00)$	$32.56^{+3.39}_{-4.02}$	$32.56^{+4.66}_{-5.57}$	$32.78^{+3.49}_{-4.05}$	$32.78^{+4.62}_{-5.79}$
L (MeV)	$\mathcal{U}(0.0,140.0)$	$48.8^{+33.8}_{-30.6}$	$48.8^{+61.0}_{-41.8}$	$44.6^{+24.2}_{-27.8}$	$44.6^{+39.4}_{-38.1}$
K_{sym} (MeV)	$\mathcal{U}(-600.0,200.0)$	$-283.8^{+196.0}_{-188.3}$	$-283.8^{+325.4}_{-268.2}$	$-328.3^{+175.2}_{-169.4}$	$-328.3^{+288.3}_{-236.3}$
$f_{\sigma,\infty}$	$\mathcal{U}(0.150,1.100)$	$0.753^{+0.095}_{-0.093}$	$0.753^{+0.195}_{-0.296}$	$0.716^{+0.059}_{-0.048}$	$0.716^{+0.093}_{-0.077}$
$f_{\omega,\infty}$	$\mathcal{U}(0.150,1.600)$	$0.737^{+0.096}_{-0.086}$	$0.737^{+0.164}_{-0.347}$	$0.694^{+0.072}_{-0.048}$	$0.694^{+0.112}_{-0.070}$
$f_{\rho,\infty}$	$\mathcal{U}(0.050,1.100)$	$0.367^{+0.252}_{-0.203}$	$0.367^{+0.395}_{-0.279}$	$0.342^{+0.264}_{-0.198}$	$0.342^{+0.424}_{-0.261}$
Δd_σ	$\mathcal{U}(-1.200,1.200)$	$0.174^{+0.348}_{-0.369}$	$0.174^{+0.636}_{-0.658}$	$0.315^{+0.272}_{-0.300}$	$0.315^{+0.436}_{-0.542}$
Δd_ω	$\mathcal{U}(-1.200,1.200)$	$0.680^{+0.270}_{-0.634}$	$0.680^{+0.403}_{-1.634}$	$0.813^{+0.229}_{-0.307}$	$0.813^{+0.323}_{-0.588}$

CPC Accepted

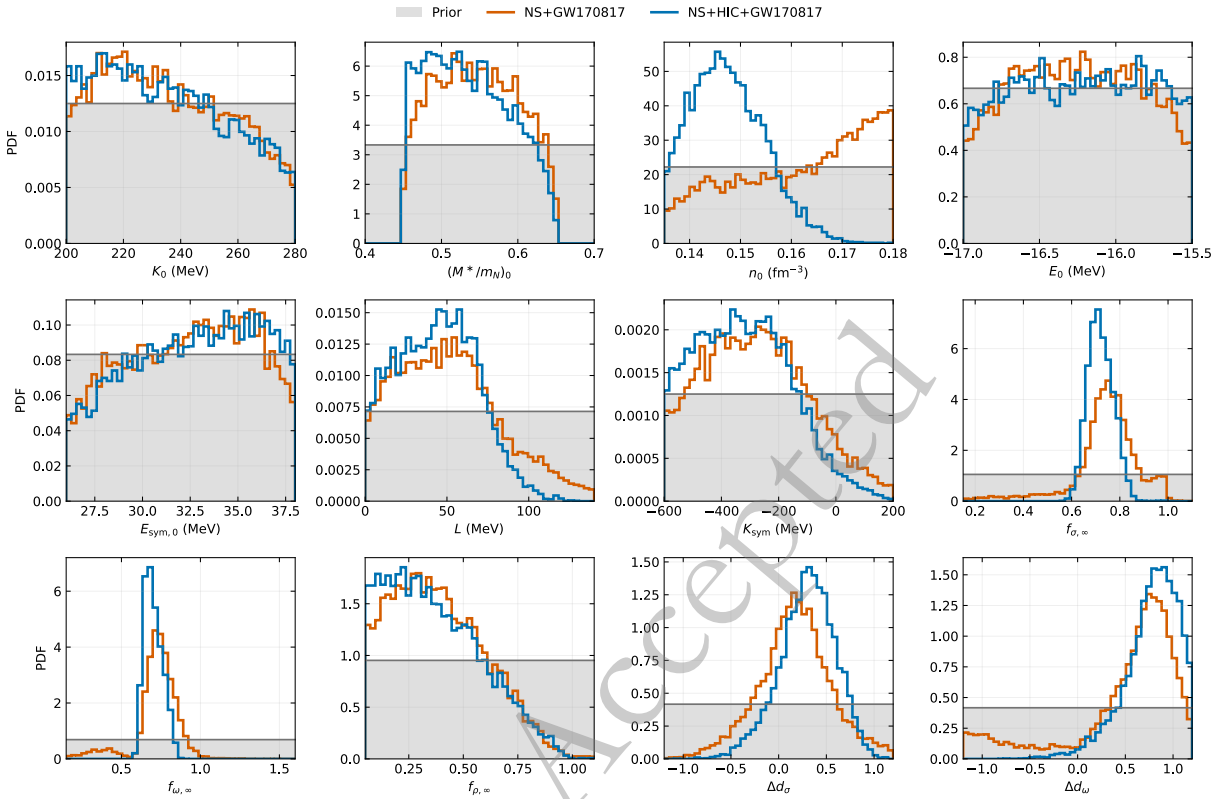

Fig. 1. (color online) One-dimensional marginalized posteriors for the 12 inferred parameters. The gray bands indicate the uniform prior ranges, while the colored curves compare the NS+GW170817 and NS+HIC+GW170817 posterior distributions.

CPC Accepted

The strongest response to the HIC constraint appears in the high-density isoscalar sector. The NS+GW170817 posterior allows a broader range of scalar and vector asymptotic limits, whereas NS+HIC+GW170817 narrows them to $f_{\sigma,\infty} = 0.716^{+0.059}_{-0.048}$ and $f_{\omega,\infty} = 0.694^{+0.072}_{-0.048}$ at 68% credibility. The vector shift offset is also pushed to positive values, $\Delta d_\omega = 0.813^{+0.229}_{-0.307}$, while Δd_σ remains compatible with a broader interval. These trends indicate that the HIC pressure band primarily selects how the scalar attraction and vector repulsion evolve above saturation, rather than fixing a single saturation parameter in isolation.

B. Reconstructed microphysics: density-dependent couplings

We now map the inferred macroscopic parameters back to microscopic interaction channels by reconstructing the density-dependent coupling shape functions $f_i(n) = g_i(n)/g_i(n_0)$ for the scalar (σ), vector (ω), and isovector (ρ) mesons. Figure 4 compares the physically accepted prior band, the NS+GW170817 posterior, and the NS+HIC+GW170817 posterior bands.

The NS+GW170817 data leave the reconstructed couplings relatively broad, particularly in the isoscalar sector. This reflects the fact that neutron-star radii, masses, and tidal deformabilities constrain the total beta-equilibrated pressure but do not uniquely determine its decomposition into scalar attraction and vector repulsion. The NS+HIC+GW170817 analysis significantly reduces the allowed region for $f_\sigma(n)$ and $f_\omega(n)$ at suprasaturation densities. This is the main microscopic impact of the HIC likelihood: the flow constraint probes the pressure generated by symmetric matter and therefore selects a narrower balance between scalar attraction and vector repulsion. The two channels remain correlated, because the large scalar and vector self-energies must change together so that their net contribution yields a pressure compatible with the HIC symmetric-matter band, the NICER mass–radius information, and GW170817. In the matched posterior comparison, the Pearson correlation between $f_{\sigma,\infty}$ and $f_{\omega,\infty}$ is $r = 0.923$ for the 12D baseline and $r = 0.975$ for the 10D matched control. The positive scalar–vector correlation is therefore present in both models, and the independent offsets in the 12D model broaden the allowed correlation structure without removing the common scalar–vector response selected by the HIC and neutron-star data.

The isovector coupling $f_\rho(n)$ remains less tightly constrained than the two isoscalar couplings. This hierarchy is physically expected: HIC enters through symmetric nuclear matter, while the NS likelihood sees the isovector sector only through beta equilibrium and the resulting pressure. The broad residual uncertainty in $f_\rho(n)$

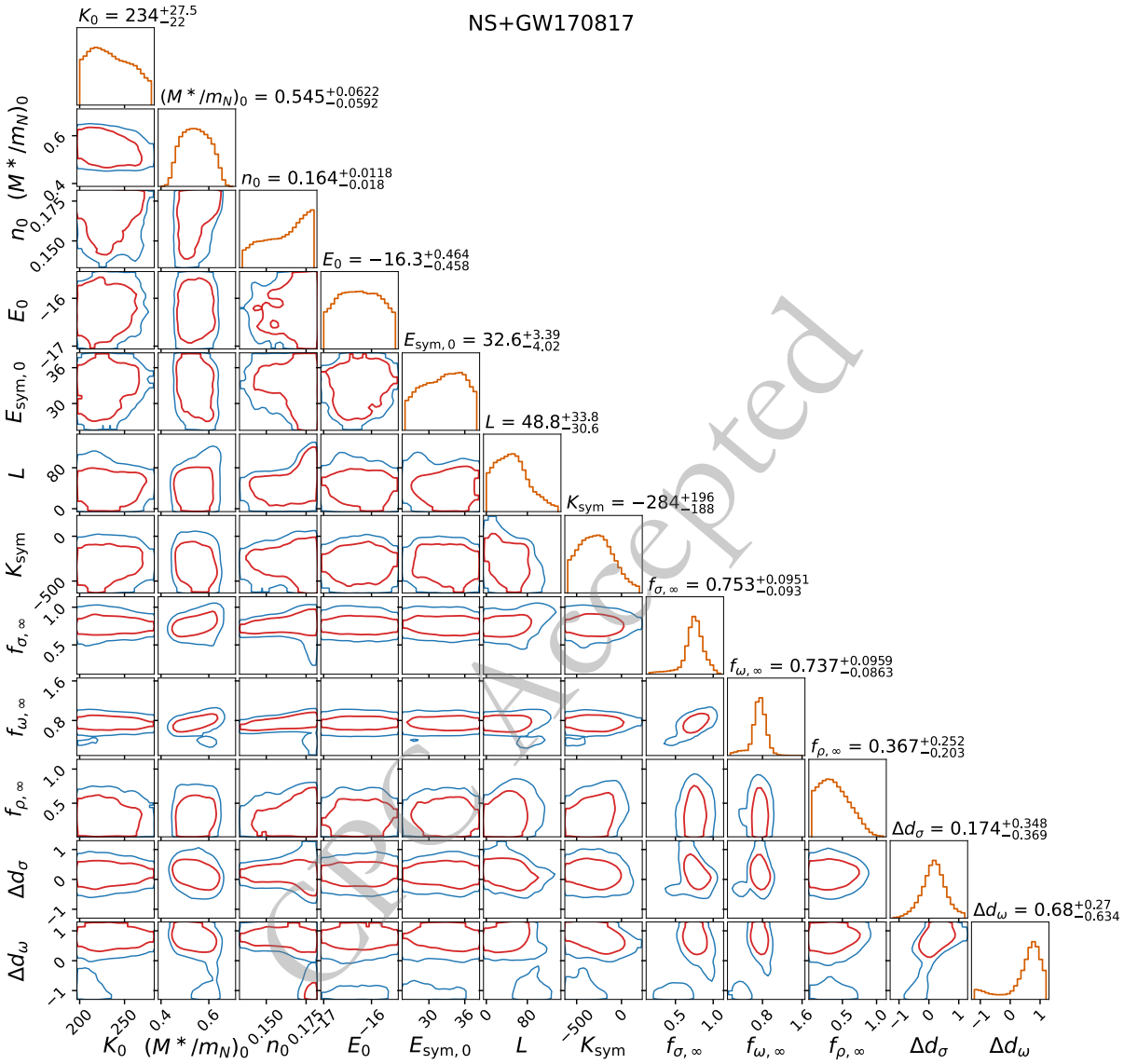

CPC Accepted

Fig. 2. (color online) Corner plot for the NS+GW170817 posterior in the 12-parameter inverse-mapped DD-RMF model. Diagonal panels show one-dimensional marginalized posteriors, and off-diagonal panels show two-dimensional joint posteriors.

should therefore be interpreted as a genuine limitation of the present data combination rather than as a numerical artifact.

C. Equation of state and the speed of sound

Translating the reconstructed couplings into thermodynamic observables, Fig. 5 compares $E_{\mathrm{sym}}(n)$, $P_\beta(n)$, the symmetric-matter energy, and $P_{\mathrm{SNM}}(n)$ for the two GW-conditioned posterior ensembles. The HIC likelihood acts directly on P_{SNM}, and the corresponding HIC+NS+GW170817 posterior band follows the HIC flow region over the densities where the constraint is applied. Through the correlated scalar and vector mean fields, this isoscalar information also propagates into the beta-equilibrated pressure relevant for neutron stars. Thus the reduction of the beta-equilibrated pressure uncertainty is a derived consequence of the selected isoscalar mean-field dynamics, not an independent HIC constraint on neutron-star matter.

The squared speed of sound, shown in Fig. 6, remains causal for the accepted posterior samples. The HIC+NS+GW170817 posterior tends to reduce the high-density spread relative to NS+GW170817, especially in the density interval where the HIC constraint compresses the isoscalar pressure. The conformal value $c_s^2 = 1/3$ is crossed at a few times saturation density for a substantial part of the posterior, indicating nonconformal stiffening in the density range relevant for massive neutron-star cores [24, 25, 80, 81].

D. Macroscopic observables: neutron-star structure

The reconstructed interaction is further tested through

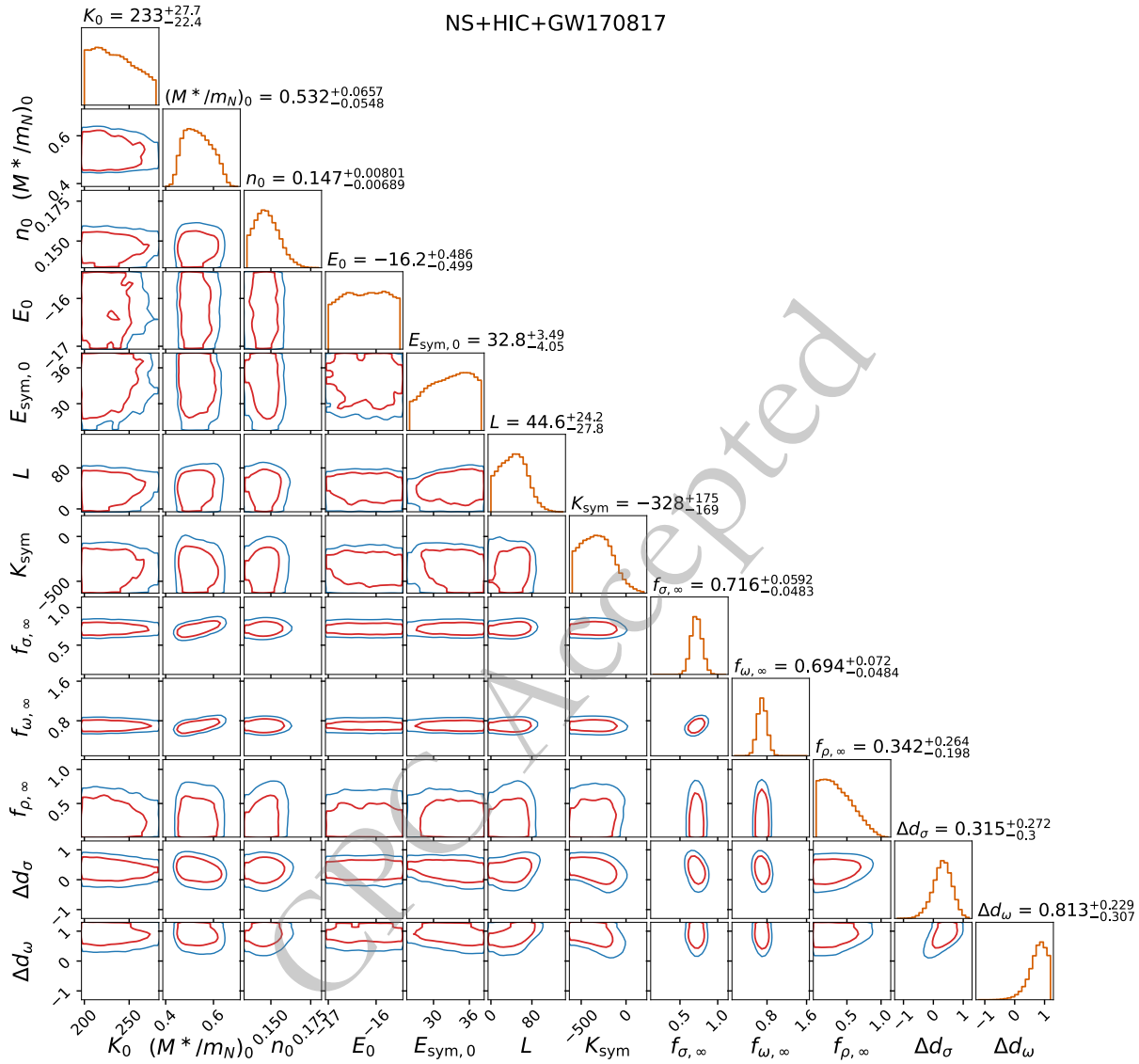

CPC Accepted

Fig. 3. (color online) Corner plot for the NS+HIC+GW170817 posterior in the 12-parameter inverse-mapped DD-RMF model. The HIC constraint narrows the high-density isoscalar sector and reveals correlations among $f_{\sigma,\infty}$, $f_{\omega,\infty}$, Δd_σ, and Δd_ω.

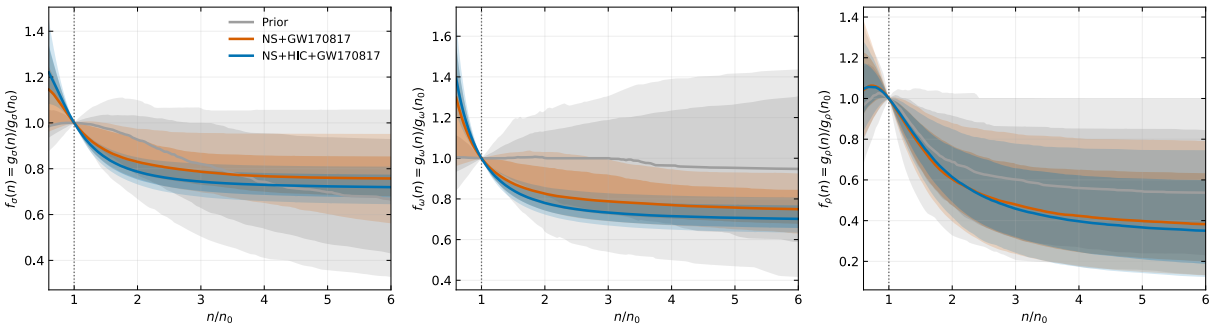

Fig. 4. (color online) Reconstructed coupling shape functions in the 12-parameter DD-RMF model. The figure compares the physically accepted prior, NS+GW170817 posterior, and NS+HIC+GW170817 posterior bands for the scalar, vector, and isovector channels.

neutron-star structure. Figure 7 shows the M–R credible regions together with NICER observational contours. For PSR J0030+0451 we display the published Miller et al. [10] and Riley et al. [11] contours directly for comparison, while PSR J0437−4715 [17] and PSR J0740+6620 [12, 16] are shown with the same observational posterior

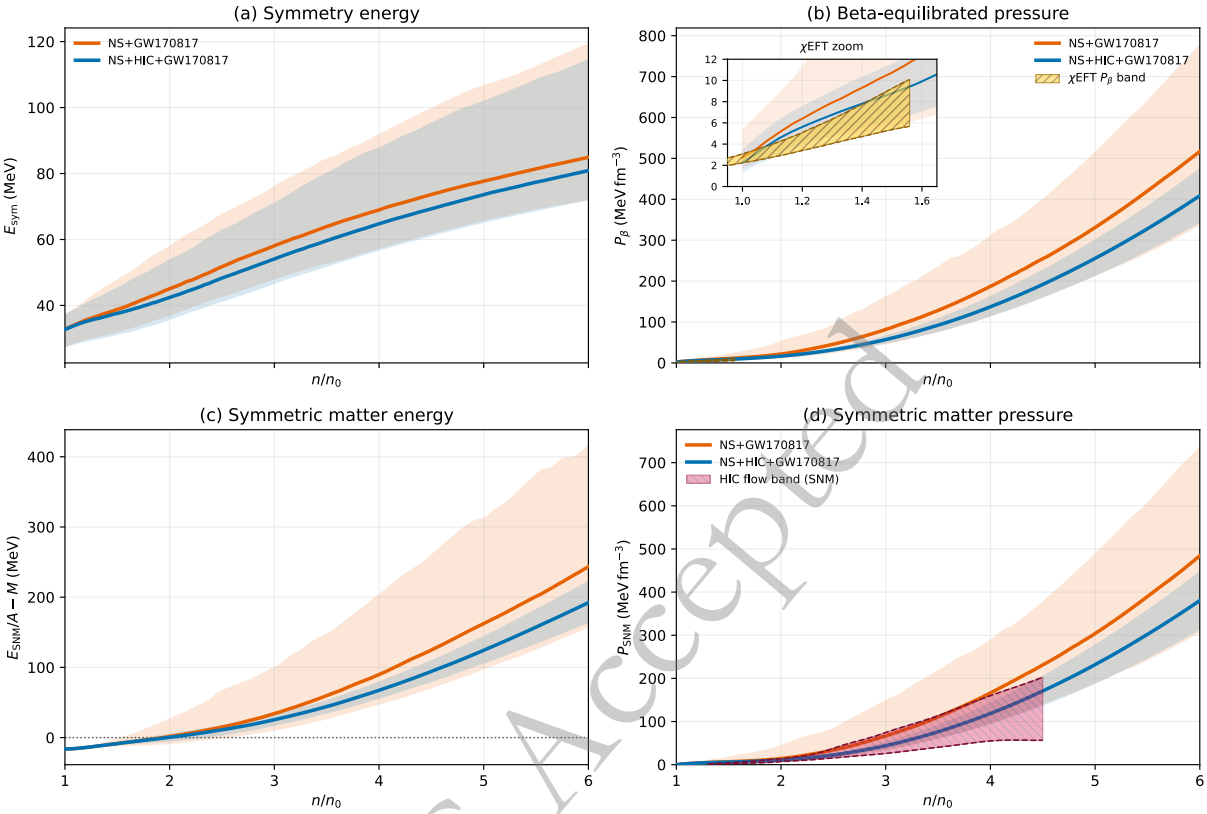

Fig. 5. (color online) Reconstructed EOS quantities for NS+GW170817 and HIC+NS+GW170817. The panels show the symmetry energy, the pressure of cold beta-equilibrated matter, the symmetric-matter energy per baryon, and the symmetric-matter pressure as functions of n/n_0. The χEFT beta-equilibrated pressure band and the HIC symmetric-matter flow band are shown as external reference bands in the corresponding pressure panels.

Table 2. Posterior-level sensitivity tests for NS+HIC+GW170817. The baseline uses $\sigma_{\rm HIC} = (P_{\rm max} - P_{\rm min})/2$. The fixed-$n_0$ row fixes only the HIC density coordinate at $n = u(0.16\,{\rm fm}^{-3})$, and the EOS saturation parameter n_0 remains sampled. The 10D matched control fixes $\Delta d_\sigma = \Delta d_\omega = 0$.

Data set	$R_{1.4}$ (km)	$R_{2.0}$ (km)	$M_{\rm max}$ ($M_\odot$)
12D baseline	$11.91^{+0.37}_{-0.37}$	$11.39^{+0.45}_{-0.51}$	$2.123^{+0.084}_{-0.074}$
12D HIC width ×2	$11.82^{+0.42}_{-0.38}$	$11.39^{+0.45}_{-0.50}$	$2.140^{+0.084}_{-0.085}$
12D fixed-n_0 HIC coordinate	$11.54^{+0.32}_{-0.27}$	$10.84^{+0.29}_{-0.33}$	$2.055^{+0.046}_{-0.046}$
10D matched control	$12.02^{+0.38}_{-0.35}$	$11.29^{+0.48}_{-0.47}$	$2.089^{+0.073}_{-0.067}$

products used in the plotting workflow. Figure 8 and Table 3 summarize the marginalized posterior distributions of $R_{1.4}$, $R_{2.0}$, and $M_{\rm max}$.

The NS+GW170817 posterior gives $R_{1.4} = 11.96^{+0.54}_{-0.49}$ km, $R_{2.0} = 11.66^{+0.72}_{-0.56}$ km, and $M_{\rm max} = 2.176^{+0.118}_{-0.090}\,M_\odot$ at 68% credibility. Adding the HIC symmetric-matter pressure constraint shifts the posterior toward slightly more compact high-mass stars and reduces the credible intervals, giving $R_{1.4} = 11.91^{+0.37}_{-0.37}$ km, $R_{2.0} = 11.39^{+0.45}_{-0.51}$ km, and $M_{\rm max} = 2.123^{+0.084}_{-0.074}\,M_\odot$. These macroscopic shifts are secondary consequences of the narrower high-density isoscalar pressure range and scalar–vector mean-field evolution selected by NS+HIC+GW170817. The quoted values are conditional on the 12-parameter DD-RMF model and on the adopted likelihood choices.

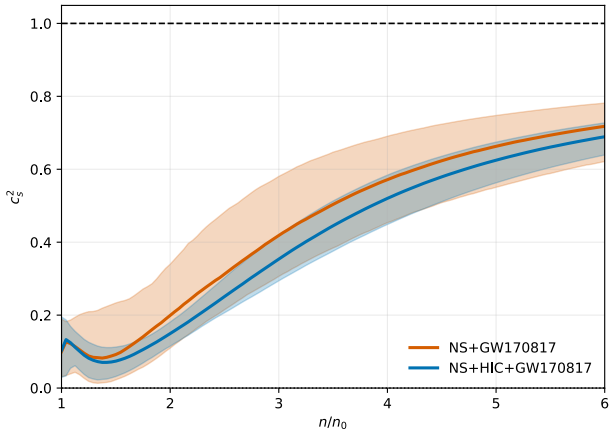

Fig. 6. (color online) Squared speed of sound $c_s^2 = dP/d\varepsilon$ for cold beta-equilibrated matter inferred from the NS+GW170817 and HIC+NS+GW170817 posterior ensembles. The dashed line marks the causality bound $c_s^2 = 1$.

Posterior-level sensitivity results are summarized in Table 2. The table compares the baseline with the

CPC Accepted

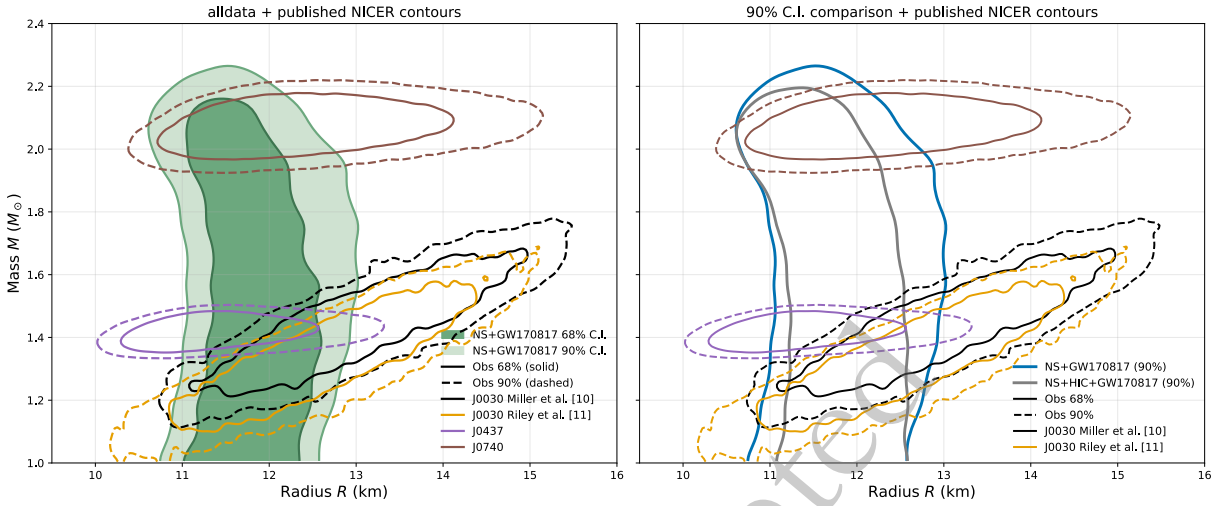

Fig. 7. (color online) Mass–radius constraints from the inverse-mapped DD-RMF inference. The left panel shows the NS+GW170817 posterior credible region together with NICER observational contours. For PSR J0030+0451, the published Miller et al. [10] and Riley et al. [11] contours are plotted directly for comparison and are not treated as two independent likelihood factors. The PSR J0437−4715 and PSR J0740+6620 contours are also shown. The right panel compares the 90% credible mass–radius envelopes from NS+GW170817 and NS+HIC+GW170817.

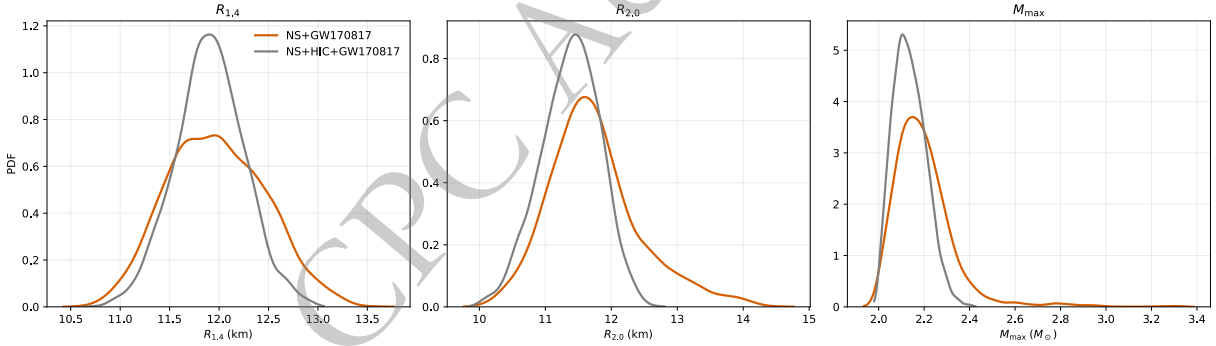

Fig. 8. (color online) Marginalized posteriors of derived neutron-star observables: $R_{1.4}$, $R_{2.0}$, and $M_{\max}$, shown for the NS+GW170817 and NS+HIC+GW170817 data selections.

Table 3. Derived neutron-star macroscopic observables inferred from the posterior EOS ensembles. For each data selection we report the 68% and 90% central credible intervals.

Data set	Observable	Unit	68% C.I.	90% C.I.
NS+GW170817	$R_{1.4}$	km	$11.96^{+0.54}_{-0.49}$	$11.96^{+0.83}_{-0.76}$
NS+GW170817	$R_{2.0}$	km	$11.66^{+0.72}_{-0.56}$	$11.66^{+1.45}_{-0.93}$
NS+GW170817	$M_{\max}$	$M_\odot$	$2.176^{+0.118}_{-0.090}$	$2.176^{+0.241}_{-0.138}$
NS+HIC+GW170817	$R_{1.4}$	km	$11.91^{+0.37}_{-0.37}$	$11.91^{+0.59}_{-0.60}$
NS+HIC+GW170817	$R_{2.0}$	km	$11.39^{+0.45}_{-0.51}$	$11.39^{+0.71}_{-0.84}$
NS+HIC+GW170817	$M_{\max}$	$M_\odot$	$2.123^{+0.084}_{-0.074}$	$2.123^{+0.134}_{-0.115}$

doubled-width HIC test, the fixed-n_0 HIC-coordinate test, and the matched 10D control. Relative to the 12D baseline, doubling the HIC width shifts the medians by −0.09 km in $R_{1.4}$, +0.005 km in $R_{2.0}$, and +0.017 $M_\odot$ in $M_{\max}$. The fixed-n_0 coordinate test shifts them by −0.37 km, −0.54 km, and −0.067 $M_\odot$, respectively, while the 10D matched control shifts them by +0.10 km, −0.10 km, and −0.033 $M_\odot$. The fixed-n_0 shifts are comparable to the baseline 68% uncertainties: 0.37 km for $R_{1.4}$ and approximately 0.45–0.51 km for $R_{2.0}$. Moreover, its 0.54 km shift in $R_{2.0}$ exceeds the 0.27 km change from 11.66 to 11.39 km obtained when HIC is added to the NS+GW170817 baseline. The direction of the response toward smaller radii is unchanged, but its magnitude depends materially on the density-coordinate convention. Consequently, the precise HIC-conditioned radius medians and their sub-kilometer differences should be regarded as conditional on this convention, rather than as robust HIC-only constraints. The width test remains stable, and the extra offset freedom produces only modest changes in the shared macroscopic predictions.

The corresponding principal-parameter medians are also stable. The 12D baseline gives $n_0 = 0.1470\,\mathrm{fm}^{-3}$,

CPC Accepted

$L = 44.58$ MeV, $K_{\rm sym} = -328.32$ MeV, $f_{\sigma,\infty} = 0.716$, and $f_{\omega,\infty} = 0.694$. The HIC-width-×2 test gives $0.1480\,\mathrm{fm}^{-3}$, 46.79 MeV, −316.19 MeV, 0.731, and 0.701, while the fixed-n_0 coordinate test gives $0.1541\,\mathrm{fm}^{-3}$, 45.80 MeV, −286.98 MeV, 0.714, and 0.687, respectively. The parameter shifts likewise show that the qualitative scalar–vector response persists, while its quantitative posterior location remains sensitive to the HIC density-coordinate choice.

IV. CONCLUSIONS

We have developed a Bayesian inference framework for the EOS of cold dense matter within a 12-parameter inverse-mapped DD-RMF model. The sampled parameters include saturation-scale nuclear-matter properties, three asymptotic coupling limits, and two independent isoscalar shift offsets, Δd_σ and Δd_ω. This parametrization keeps the EOS connected to microscopic scalar, vector, and isovector interaction channels while allowing a flexible high-density isoscalar evolution.

Combining NICER, GW170817, and HIC information within the inverse-mapped DD-RMF model narrows the high-density isoscalar sector and selects correlated scalar and vector coupling functions. This channel-level constraint propagates to the neutron-star mass–radius relation. The posterior comparisons support the qualitative scalar–vector response, while the fixed-n_0 test shows that its quantitative radius implications depend on the adopted HIC density-coordinate conversion.

Causality is imposed through the physical viability filter, and all accepted posterior EOS samples satisfy the causal sound-speed condition. The sound speed can exceed the conformal value at a few times saturation density, reflecting the nonconformal stiffening needed to support massive neutron stars while satisfying the HIC-selected intermediate-density pressure. Future work should reduce the density-coordinate systematic and test broader high-density parametrizations, additional multimessenger events, and hierarchical neutron-star mass distributions [79].

Appendix A: Inverse mapping of the DD-RMF parameters

In this appendix, we detail the inverse mapping procedure used to reconstruct the coupling strengths G_{i0} and the density-dependence shape functions $f_i(n)$ from the 12-dimensional parameter vector $\boldsymbol{\theta}$ defined in Eq. (7). The first three steps fix the coupling strengths at saturation algebraically. The fourth step is a coupled numerical solution for the density-shape parameters of all three channels.

Step 1: Fix $G_{\sigma0}$ from $(M^*/m_N)_0$. At the saturation density $n = n_0$ in symmetric nuclear matter (SNM, $n_n = n_p = n_0/2$), we compute the Fermi momentum k_{F0} and the scalar density n_{s0} using Eq. (1) and the definition of the effective mass with $M_0^* = (M^*/m_N)_0\, m_N$. The scalar coupling strength at saturation is then given by

$$G_{\sigma0} = \frac{m_N - M_0^*}{n_{s0}}. \tag{A1}$$

Step 2: Fix $G_{\omega0}$ from E_0 and the SNM energy at saturation. Using the kinetic energy density $\varepsilon_{N,0}$ at $(n_0/2, n_0/2)$, we enforce the energy per baryon in SNM to reproduce the binding energy E_0:

$$\frac{\varepsilon(n_0,0)}{n_0} = m_N + E_0 = \frac{\varepsilon_{N,0}}{n_0} + \frac{1}{2}G_{\sigma0}\frac{n_{s0}^2}{n_0} + \frac{1}{2}G_{\omega0}\,n_0. \tag{A2}$$

This yields the vector coupling strength:

$$G_{\omega0} = \frac{2}{n_0}\left[(m_N + E_0) - \frac{\varepsilon_{N,0}}{n_0} - \frac{1}{2}G_{\sigma0}\frac{n_{s0}^2}{n_0}\right]. \tag{A3}$$

Step 3: Fix $G_{\rho0}$ from $E_{\rm sym,0}$. Using the standard mean-field decomposition for the symmetry energy,

$$E_{\rm sym}(n) = E_{\rm sym}^{\rm kin}(n) + \frac{1}{2}G_\rho(n)\,n, \tag{A4}$$

where $E_{\rm sym}^{\rm kin}(n_0) = k_{F0}^2/(6E_{F0}^*)$, we obtain the isovector coupling strength:

$$G_{\rho0} = \frac{2}{n_0}\left[E_{\rm sym,0} - E_{\rm sym,0}^{\rm kin}\right]. \tag{A5}$$

Step 4: Determine the density-shape parameters in Eq. (6). The isovector and isoscalar matching relations below specify a single coupled problem. Their order of presentation does not imply that the ρ channel is fixed before the scalar density dependence.

(i) Isovector channel ρ: matching $(L, K_{\rm sym})$. We write $G_\rho(n) = G_{\rho0} f_\rho^2(n)$ and define the first and second derivatives with respect to $x = n/n_0$ at saturation:

$$\eta_\rho \equiv \left.\frac{df_\rho}{dx}\right|_{x=1}, \qquad \kappa_\rho \equiv \left.\frac{d^2 f_\rho}{dx^2}\right|_{x=1}. \tag{A6}$$

Using Eq. (A4) and the normalization $f_\rho(1) = 1$, we find

$$\left.\frac{dE_{\rm sym}}{dn}\right|_{n_0} = \left.\frac{dE_{\rm sym}^{\rm kin}}{dn}\right|_{n_0} + \frac{1}{2}G_{\rho0}\left(1 + 2\eta_\rho\right), \tag{A7}$$

$$\left.\frac{d^2E_{\rm sym}}{dn^2}\right|_{n_0} = \left.\frac{d^2E_{\rm sym}^{\rm kin}}{dn^2}\right|_{n_0} + \frac{G_{\rho0}}{n_0}\left(2\eta_\rho + \eta_\rho^2 + \kappa_\rho\right). \tag{A8}$$

CPC Accepted

Inverting these relations gives the required derivatives:

$$\eta_\rho = \frac{1}{2}\left[\frac{\dfrac{L}{3n_0} - \left.\dfrac{dE_{\rm sym}^{\rm kin}}{dn}\right|_{n_0}}{\dfrac{1}{2}G_{\rho 0}} - 1\right], \tag{A9}$$

$$\kappa_\rho = \left(\frac{K_{\rm sym}}{9n_0^2} - \left.\frac{d^2E_{\rm sym}^{\rm kin}}{dn^2}\right|_{n_0}\right)\frac{n_0}{G_{\rho 0}} - \left(2\eta_\rho + \eta_\rho^2\right). \tag{A10}$$

We then determine $(a_\rho, b_\rho, c_\rho, d_\rho)$ by solving the four constraints at $x = 1$:

$$f_\rho(1) = 1, \qquad f_{\rho,\infty} = f_{\rho,\infty}^{(\rm input)}, \qquad \left.\frac{df_\rho}{dx}\right|_1 = \eta_\rho, \qquad \left.\frac{d^2f_\rho}{dx^2}\right|_1 = \kappa_\rho, \tag{A11}$$

These conditions are imposed together with the isoscalar constraints. Equations (A9) and (A10) are conditional identities for a given scalar density dependence, not a prescription for solving the ρ channel independently. In particular, the derivatives of $E_{\rm sym}^{\rm kin}$ change when the trial scalar shape changes.

In the numerical residual evaluation, the full symmetry energy is computed as

$$E_{\rm sym}(n) = \frac{k_F(n)^2}{6\sqrt{k_F(n)^2 + M^*(n)^2}} + \frac{1}{2}G_{\rho 0}f_\rho(n)^2 n, \tag{A12}$$

where $M^*(n)$ is obtained by solving the scalar field equation using the current trial $G_{\sigma 0}f_\sigma(n)^2$ at that density. Values are evaluated at $n_j = n_0(1+z_j)$ with $z_j = hj$, $j = -3,\ldots,3$, and $h = 0.008$. A degree-five polynomial $S(z) = \sum_{k=0}^{5} s_k z^k$ is fitted to these seven values. The residuals use $E_{\rm sym}(n_0) \simeq s_0$, $L \simeq 3s_1$, and $K_{\rm sym} \simeq 18s_2$. This procedure includes the density response of the effective mass through its self-consistent solution at each stencil point. The closed-form kinetic-symmetry-energy derivatives obtained from the saturation effective mass are used only to construct an initial guess for the ρ-channel parameters. They are not used as the final L or $K_{\rm sym}$ residuals.

(ii) Isoscalar channels σ,ω: matching $(P(n_0) = 0, K_0)$. The scalar and vector shifts are parameterized by two sampled offsets, Δd_σ and Δd_ω, relative to the isovector shift. We write

$$d_\sigma = d_\rho + \Delta d_\sigma, \qquad d_\omega = d_\rho + \Delta d_\omega. \tag{A13}$$

For a specified pair $(\Delta d_\sigma, \Delta d_\omega)$, we enforce the asymptotic values $f_{\sigma,\infty}$ and $f_{\omega,\infty}$ through the reduced forms

$$f_i(x) = a_i\frac{1 + b_i(x+d)^2}{1 + c_i(x+d)^2},$$
$$a_i = 1 + c_i(1+d)^2(1 - f_{i,\infty}), \qquad b_i = \frac{f_{i,\infty}\,c_i}{a_i}, \tag{A14}$$

where $d = d_i$ for each isoscalar channel, i.e. $d = d_\sigma$ for $i = \sigma$ and $d = d_\omega$ for $i = \omega$. This keeps $f_i(1) = 1$ and $f_i(\infty) = f_{i,\infty}$ satisfied identically while allowing the scalar and vector density-dependence shapes to move independently. The remaining unknowns are determined numerically by enforcing the SNM thermodynamic conditions at saturation together with the isovector constraints in Eq. (A11):

$$P(n_0, 0) = 0, \qquad K_0 = 9\left.\frac{dP(n,0)}{dn}\right|_{n_0}. \tag{A15}$$

If the derivative is instead taken with respect to the dimensionless variable $u = n/n_0$, the equivalent expression is $K_0 = (9/n_0)\,dP/du|_{u=1}$. In evaluating $P(n,0)$, the rearrangement contribution is explicitly included:

$$P(n,0) = P_N(n,0) + \frac{1}{2}G_\omega(n)n^2 - \frac{1}{2}G_\sigma(n)n_s^2 + n\Sigma_R(n), \tag{A16}$$

For the definition in Eq. (A15), a symmetric finite-difference estimate with $\Delta n = 10^{-4}n_0$ is

$$K_0 \approx 9\,\frac{P(n_0 + \Delta n, 0) - P(n_0 - \Delta n, 0)}{2\Delta n}. \tag{A17}$$

After eliminating $a_\sigma, b_\sigma, a_\omega, b_\omega$ through Eq. (A14), the six numerical unknowns are $(c_\sigma, c_\omega, a_\rho, b_\rho, c_\rho, d_\rho)$. They are varied jointly to match the pressure and incompressibility conditions, L, $K_{\rm sym}$, $f_\rho(1) = 1$, and the sampled $f_{\rho,\infty}$. The sampled offsets set d_σ and d_ω through Eq. (A13). Every residual evaluation therefore uses the same trial scalar background in both the isoscalar and isovector conditions. The bounded nonlinear solve uses the standard least-squares stopping criteria: xtol is the relative parameter-step tolerance, ftol is the relative decrease tolerance for the residual cost, and gtol is the gradient-based optimality tolerance. In the production calculation, all three are set to 10^{-9}, with a maximum of 500 residual-function evaluations for each initial guess.

The production acceptance thresholds on the internal diagnostics were 0.08 MeV fm^{-3} for $|P(n_0)|$, 8 MeV for the incompressibility residual, 0.08 MeV for the symmetry-energy residual, 2 MeV for the slope residual, and 12 MeV for the symmetry-energy curvature residual. The dimensionless thresholds on $|f_\rho(1) - 1|$ and $|f_{\rho,\infty}^{\rm reconstructed} - f_{\rho,\infty}^{\rm input}|$ were 0.01 and 0.02, respectively. These are rejection thresholds, not estimates of finite-difference truncation error or nonlinear-solver convergence tolerances.

CPC Accepted

Re-evaluating these internal diagnostics for all 10,662 baseline posterior samples produced 10,662 finite audit rows. The reported maximum absolute residuals were $0.0344\,\mathrm{MeV\,fm^{-3}}$ for the pressure, 7.97 MeV for the internal incompressibility diagnostic, 0.0799 MeV for the symmetry energy, 2.00 MeV for its slope, and 12.0 MeV for its curvature; the two dimensionless ρ-channel residuals were 0.00532 and 0.00554. This internal check establishes compliance with the implemented rejection thresholds. For the numerical-sensitivity check, the likelihood was recomputed for all 10,662 baseline posterior samples under tighter nonlinear-solver tolerances and alternative derivative steps, followed by importance reweighting. Tightening to $\mathrm{xtol} = \mathrm{ftol} = \mathrm{gtol} = 10^{-11}$, with $\mathrm{max_nfev} = 2000$ denoting the maximum number of residual-function evaluations, gave an effective sample size of 10,654.9 out of 10,655 finite pairs; the largest posterior-median shift was 0.0029 MeV in L. Changing the symmetry-energy stencil from $h = 0.008$ to $h = 0.004$ and $h = 0.016$ gave effective sample sizes of 9,385.3 and 9,538.7, with a largest median shift of 0.95 MeV in K_{sym} and a largest 90% endpoint shift of 8.07 MeV. Changing the pressure-derivative step from $\Delta n = 10^{-4} n_0$ to $5\times10^{-5} n_0$ and $2\times10^{-4} n_0$ gave effective sample sizes of 10,623.0 and 10,623.8; the largest median shifts were 0.0053 MeV in L and 0.0225 MeV in K_{sym}. These tests leave the reported physical conclusions unchanged.

Auditing the maximum residuals under these alternative settings gave $(\max|K_0\,\mathrm{residual}|, \max|K_{\mathrm{sym}}\,\mathrm{residual}|) = (7.9665, 11.9974)$ MeV for the baseline, $(7.9665, 11.9974)$ MeV for the tighter solver tolerances, $(7.9654, 11.9967)$ MeV for $h/2$, $(7.9853, 11.9938)$ MeV for $2h$, $(7.9666, 11.9954)$ MeV for $\Delta n/2$, and $(7.9665, 11.9970)$ MeV for $2\Delta n$. The alternative settings yielded 3–12 failed reconstructions out of 10,662 samples, and the valid rows remained within the stated production thresholds. These results show that the approximately 8 MeV and 12 MeV values reflect the implemented acceptance limits, rather than errors removed by tightening the numerical settings.

Appendix B: Pressure-band data for comparison and HIC likelihood

For reproducibility of the production likelihood, Table 4 lists the 15 pressure-band points actually used in the calculation. The grid begins at $u = 2.0$ and ends at $u = 4.5$. The boundaries are obtained by linear interpolation of the supplied pressure-band data and evaluated at 15 equally spaced points. These points are a numerical discretization of the continuous flow band, rather than 15 independent experimental measurements.

Table 4. HIC pressure-band values for symmetric nuclear matter used in the fiducial likelihood. The density coordinate is the reduced density $u = n/n_0$, and the pressure is in $\mathrm{MeV\,fm^{-3}}$. The 15 equally spaced points between $u = 2.0$ and $u = 4.5$ are obtained by linear interpolation of the pressure-band input associated with Ref. [44].

u	$P_{\min}$	$P_{\max}$	u	$P_{\min}$	$P_{\max}$
2.0000	7.4000	13.4000	3.4286	38.2286	107.5286
2.1786	9.6000	19.0929	3.6071	43.4214	123.3786
2.3571	12.7000	27.4857	3.7857	49.0429	140.3429
2.5357	16.4500	40.8857	3.9643	54.2071	156.8857
2.7143	20.0857	53.7000	4.1429	56.6714	172.1143
2.8929	23.6571	65.6929	4.3214	56.7357	186.8429
3.0714	27.8571	80.3857	4.5000	56.5000	202.6000
3.2500	33.0000	93.6500			

CPC Accepted

References

[1] J. R. Oppenheimer, G. M. Volkoff, Phys. Rev. **55**, 374 (1939)
[2] T. Hinderer, The Astrophys. J. **677**, 1216 (2008)
[3] E. E. Flanagan, T. Hinderer, Phys. Rev. D **77**, 021502 (2008)
[4] F. Özel, P. Freire, Annu. Rev. Astron. Astrophys. **54**, 401 (2016)
[5] J. M. Lattimer, M. Prakash, Phys. Reports **621**, 127 (2016)
[6] M. Oertel, M. Hempel, T. Klähn, *et al.*, Rev. Mod. Phys. **89**, 015007 (2017)
[7] P. B. Demorest, T. Pennucci, S. Ransom, *et al.*, Nat. **467**, 1081 (2010)
[8] H. T. Cromartie, *et al.*, Nat. Astron. **4**, 72 (2020)
[9] E. Fonseca, *et al.*, Astrophys. J. Lett. **915**, L12 (2021)
[10] M. C. Miller, *et al.*, The Astrophys. J. Lett. **887**, L24 (2019)
[11] T. E. Riley, *et al.*, The Astrophys. J. Lett. **887**, L21 (2019)
[12] T. E. Riley, *et al.*, The Astrophys. J. Lett. **918**, L27 (2021)
[13] M. C. Miller, *et al.*, The Astrophys. J. Lett. **918**, L28 (2021)
[14] G. Raaijmakers, *et al.*, The Astrophys. J. Lett. **918**, L29 (2021)
[15] T. Salmi, *et al.*, The Astrophys. J. **941**, 150 (2022)
[16] T. Salmi, *et al.*, The Astrophys. J. **974**, 294 (2024)
[17] D. Choudhury, T. Salmi, S. Vinciguerra, *et al.*, The Astrophys. J. Lett. **971**, L20 (2024)
[18] L. Brandes, W. Weise, Phys. Rev. D **111**, 034005 (2025)
[19] M. Koehn, *et al.*, Phys. Rev. X **15**, 021014 (2025)
[20] B. P. Abbott, *et al.*, Phys. Rev. Lett. **119**, 161101 (2017)
[21] B. P. Abbott, *et al.*, Phys. Rev. Lett. **121**, 161101 (2018)
[22] B. P. Abbott, *et al.*, The Astrophys. J. Lett. **892**, L3 (2020)
[23] R. Abbott, *et al.*, Phys. Rev. X **13**, 041039 (2023)
[24] P. Bedaque, A. W. Steiner, Phys. Rev. Lett. **114**, 031103 (2015)
[25] E. Annala, T. Gorda, A. Kurkela, *et al.*, Nat. Phys. **16**(9), 907 (2020)
[26] S. Altiparmak, C. Ecker, L. Rezzolla, Astrophys. J. Lett. **939**(2), L34 (2022)
[27] P. Landry, R. Essick, K. Chatziioannou, Phys. Rev. D **101**, 123007 (2020)

[28] R. Essick, I. Tews, P. Landry, *et al.*, Phys. Rev. Lett. **127**, 192701 (2021)
[29] P. T. H. Pang, L. Sivertsen, R. Somasundaram, *et al.*, Phys. Rev. C **109**, 025807 (2024)
[30] N. Rutherford, M. Mendes, I. Svensson, *et al.*, The Astrophys. J. Lett. **971**(1), L19 (2024)
[31] Y. Fujimoto, K. Fukushima, L. D. McLerran, *et al.*, Phys. Rev. Lett. **129**, 252702 (2022)
[32] Y. Fujimoto, K. Fukushima, K. Hotokezaka, *et al.*, Phys. Rev. Lett. **130**, 091404 (2023)
[33] K. Hebeler, J. M. Lattimer, C. J. Pethick, *et al.*, Phys. Rev. Lett. **105**, 161102 (2010)
[34] K. Hebeler, J. M. Lattimer, C. J. Pethick, *et al.*, The Astrophys. J. **773**, 11 (2013)
[35] C. Drischler, J. W. Holt, C. Wellenhofer, Annu. Rev. Nucl. Part. Sci. **71**, 403 (2021)
[36] C. Drischler, J. A. Melendez, R. J. Furnstahl, *et al.*, Phys. Rev. C **102**, 054315 (2020)
[37] J. Keller, *et al.*, Phys. Rev. Lett. **130**, 072701 (2023)
[38] Y. Lim, A. Schwenk, Phys. Rev. C **109**, 035801 (2024)
[39] N. B. Zhang, B. J. Cai, B. A. Li, *et al.*, Nucl. Sci. Tech. **28**, 1 (2017)
[40] N. B. Zhang, B. A. Li, J. Xu, The Astrophys. J. **859**, 90 (2018)
[41] W. J. Xie, B. A. Li, Astrophys. J. **883**(2), 174 (2019)
[42] Y. Zhang, M. Liu, C. J. Xia, *et al.*, Phys. Rev. C **101**, 034303 (2020)
[43] B. A. Li, L. W. Chen, C. M. Ko, Phys. Rep. **464**, 113 (2008)
[44] P. Danielewicz, R. Lacey, W. G. Lynch, Sci. **298**, 1592 (2002)
[45] P. Russotto, *et al.*, Phys. Rev. C **94**, 034608 (2016)
[46] J. Xu, L. W. Chen, M. B. Tsang, *et al.*, Phys. Rev. C **93**, 044609 (2016)
[47] B. J. Cai, L. W. Chen, Nucl. Sci. Tech. **28**, 185 (2017)
[48] A. Sørensen, *et al.*, Prog. Part. Nucl. Phys. **134**, 104080 (2024)
[49] S. Huth, *et al.*, Nat. **606**, 276 (2022)
[50] H. Yu, D. Q. Fang, Y. G. Ma, Nucl. Sci. Tech. **31**, 61 (2020)
[51] N. B. Zhang, B. A. Li, Nucl. Sci. Tech. **29**, 178 (2018)
[52] J. Liu, C. Gao, N. Wan, *et al.*, Nucl. Sci. Tech. **32**, 117 (2021)
[53] D. Adhikari, *et al.*, Phys. Rev. Lett. **126**, 172502 (2021)
[54] D. Adhikari, *et al.*, Phys. Rev. Lett. **129**, 042501 (2022)
[55] W. J. Xie, Z. W. Ma, J. H. Guo, Nucl. Sci. Tech. **34**(6), 91 (2023)
[56] J. D. Walecka, Annals Phys. **83**, 491 (1974)
[57] J. Boguta, A. R. Bodmer, Nucl. Phys. A **292**, 413 (1977)
[58] B. D. Serot, J. D. Walecka, Int. J. Mod. Phys. E **6**, 515 (1997)
[59] P. Ring, Prog. Part. Nucl. Phys. **37**, 193 (1996)
[60] G. A. Lalazissis, J. König, P. Ring, Phys. Rev. C **55**, 540 (1997)
[61] B. G. Todd-Rutel, J. Piekarewicz, Phys. Rev. Lett. **95**, 122501 (2005)
[62] S. Typel, H. H. Wolter, Nucl. Phys. A **656**, 331 (1999)
[63] G. A. Lalazissis, T. Nikšić, D. Vretenar, *et al.*, Phys. Rev. C **71**, 024312 (2005)
[64] T. Nikšić, D. Vretenar, P. Ring, Phys. Rev. C **78**, 034318 (2008)
[65] W. J. Xie, C. J. Xia, C. Zhang, *et al.*, Phys. Rev. D **114**(2), 023016 (2026)
[66] W. J. Xie, C. J. Xia, Nucl. Sci. Tech. **37**(9), 161 (2026)
[67] J. Skilling, in AIP Conference Proceedings, Nested sampling, Vol. 735, 2004, pp. 395–405
[68] F. Feroz, M. P. Hobson, M. Bridges, Mon. Notices Royal Astron. Soc. **398**, 1601 (2009)
[69] S. Typel, Phys. Rev. C **71**, 064301 (2005)
[70] C. J. Xia, W. J. Xie, M. Bakhiet, Phys. Rev. D **110**, 114009 (2024)
[71] M. Dutra, O. Lourenço, S. S. Avancini, *et al.*, Phys. Rev. C **90**, 055203 (2014)
[72] M. B. Tsang, J. R. Stone, F. Camera, *et al.*, Phys. Rev. C **86**, 015803 (2012)
[73] F. Douchin, P. Haensel, Astron. Astrophys. **380**, 151 (2001)
[74] R. C. Tolman, Phys. Rev. **55**, 364 (1939)
[75] W. J. Xie, B. A. Li, N. B. Zhang, Phys. Rev. D **110**, 043025 (2024)
[76] J. Skilling, Bayesian Analysis **1**(4), 833 (2006)
[77] G. Raaijmakers, S. K. Greif, T. E. Riley, *et al.*, Astrophys. J. **893**(1), L21 (2020)
[78] J. Antoniadis, P. C. C. Freire, N. Wex, *et al.*, Sci. **340**(6131), 448 (2013)
[79] B. Biswas, S. Rosswog, Phys. Rev. D **112**, 023045 (2025)
[80] I. Tews, J. Carlson, S. Gandolfi, *et al.*, The Astrophys. J. **860**(2), 149 (2018)
[81] B. Reed, C. J. Horowitz, Phys. Rev. C **101**(4), 045803 (2020)

CPC Accepted